Journal of Materials Chemistry C

ROYAL SOCIETY OF CHEMISTRY

COMMUNICATION

View Article Online
View Journal | View Issue

Cite this: J. Mater. Chem. C, 2020, 8, 15086

Received 13th July 2020,
Accepted 7th August 2020

DOI: 10.1039/d0tc03309j

rsc.li/materials-c

Elucidating charge transport mechanisms in cellulose-stabilized graphene inks†

Ana C. M. de Moraes,‡[a] Jan Obrzut, ‡*[b] Vinod K. Sangwan,[a] Julia R. Downing,[a] Lindsay E. Chaney,[a] Dinesh K. Patel,[c] Randolph E. Elmquist[c] and Mark C. Hersam *[adef]

Solution-processed graphene inks that use ethyl cellulose as a polymer stabilizer are blade-coated into large-area thin films. Following blade-coating, the graphene thin films are cured to pyrolyze the cellulosic polymer, leaving behind an sp^2-rich amorphous carbon residue that serves as a binder in addition to facilitating charge transport between graphene flakes. Systematic charge transport measurements, including temperature-dependent Hall effect and non-contact microwave resonant cavity characterization, reveal that the resulting electrically percolating graphene thin films possess high mobility ($\approx$160 $cm^2 V^{-1} s^{-1}$), low energy gap, and thermally activated charge transport, which develop weak localization behavior at cryogenic temperatures.

Introduction

Few-layer graphene (FLG) consists of atomically thin layers of sp^2-hybridized honeycomb lattices of carbon arranged in a van der Waals stack.[1] The extended π-conjugation in the graphene network enables high mobility of charge carriers, resulting in a material with superlative electronic properties.[2–4] Unlike monolayer graphene, FLG has emerged as a practically relevant material for a wide range of scalable, low-cost, and commercial technologies.[5] While graphene can be produced by mechanical exfoliation, chemical vapor deposition, and epitaxial growth on silicon carbide, these methods lack scalability for many practical applications where low-cost, high-volume conducting films are desired.[6,7] Hence, liquid-phase exfoliation has emerged to fill this need as a scalable manufacturing approach to separate and collect highly conducting FLG flakes using shear forces that overcome weak interlayer interactions in bulk graphite crystals. Liquid-phase approaches are compatible with a diverse range of organic solvents, surfactant media, ionic liquids, and polymer solutions.[8,9]

These highly processable and stable graphene dispersions can be incorporated into ink formulations with specific physicochemical properties, such as tailored viscosity and surface wetting character,[10] which render them compatible with a variety of additive manufacturing technologies including inkjet printing, aerosol jet printing, gravure printing, screen printing, spray/spin-coating, and blade-coating.[11–13] This processing versatility enables patterning over large areas and the integration of percolating graphene thin films into printed electronic applications.[12] Of particular interest are graphene inks that are stabilized by the polymer ethyl cellulose (EC), which have achieved high conductivity patterns ($\approx 10^4$ S m^{-1}) with high mechanical flexibility, resilience, and endurance.[14–16] In addition, EC not only acts as an ink viscosity modifier but also as a dispersant and stabilizer for the exfoliation of graphene in solution.[17] Unlike traditional binders and additives whose removal leaves residues that may disrupt the conductive network,[18] the thermal decomposition of EC generates sp^2-rich carbonaceous residues that improve charge transport in the percolating network of graphene sheets.[15]

Despite the extensive exploration of charge transport in graphene produced from conventional growth methods and mechanical cleavage,[19,20] systematic studies of charge transport in printed, percolating graphene thin films are relatively rare. An early study on vacuum-filtered films of chemically exfoliated graphene flakes showed Mott variable range hopping transport *via* four-probe and magnetoresistance measurements.[21] Recently, Juntunen and coworkers[22] reported a graphene ink prepared using polyvinylpyrrolidone as a polymer additive, resulting in

[a] Department of Materials Science and Engineering, Northwestern University, Evanston, IL 60208, USA. E-mail: m-hersam@northwestern.edu
[b] Materials Science and Engineering Division, Material Measurement Laboratory, National Institute of Standards and Technology, Gaithersburg, MD 20899, USA. E-mail: jan.obrzut@nist.gov
[c] Quantum Measurements Division, Physical Measurement Laboratory, National Institute of Standards and Technology, Gaithersburg, MD 20899, USA
[d] Department of Chemistry, Northwestern University, Evanston, IL 60208, USA
[e] Department of Medicine, Northwestern University, Evanston, IL 60208, USA
[f] Department of Electrical and Computer Engineering, Northwestern University, Evanston, IL 60208, USA

† Electronic supplementary information (ESI) available. See DOI: 10.1039/d0tc03309j

‡ These authors contributed equally to this work.

spray-coated graphene films with p-type Hall mobility of $\approx$20 cm^2 V^{-1} s^{-1}. Similarly, an aqueous surfactant-stabilized graphene solution was used for inkjet printing, resulting in percolating films with charge carrier mobility of $\approx$33 cm^2 V^{-1} s^{-1}.[23] However, despite their widespread use and high electrical conductivities, the underlying charge transport mechanisms in percolating thin films based on cellulose-stabilized graphene inks remain largely unexplored.

Herein, we report the charge transport characterization of solution-processed graphene inks that use EC as a stabilizing polymer. Large-area graphene films were deposited by blade-coating and then cured to pyrolyze the EC, resulting in homogeneous, percolating films with efficient charge transport between the graphene flakes. Charge transport characteristics were probed by two different methods: temperature-dependent Hall measurements and non-contact microwave resonant cavity measurements.[24,25] Hall measurements revealed a hole mobility of $\approx$160 cm^2 V^{-1} s^{-1}, which is the highest mobility reported in solution-processed graphene films. In addition, microwave resonant cavity measurements at 7.435 GHz revealed a sheet conductance of 9.26 $\times$ 10^{-3} S. These high DC mobility and microwave sheet conductance values can be attributed to improved inter-flake charge transport that is promoted by the sp^2-rich amorphous carbon residues that remain from the pyrolyzed EC. Furthermore, variable temperature measurements above 5 K show thermally activated charge transport, similar to the semiconducting behavior of twisted multilayer and Bernal graphite samples studied elsewhere.[26,27] Interestingly, below 5 K, we also observe weak localization behavior, which has been previously observed in monolayer graphene.[28] Overall, these unprecedentedly high mobility and microwave sheet conductance responses suggest that printed films based on cellulose-stabilized graphene inks are suitable for a diverse range of applications including space materials and high-frequency flexible electronics.

Results and discussion

Graphene film preparation and characterization

Graphene (Gr) flakes were prepared by liquid-phase shear exfoliation of graphite using EC polymer as a dispersant and stabilizer, as detailed in the ESI.† The use of EC enables control over the physical properties of the graphene ink, such as viscosity and solid loading, which was formulated by direct dispersion of the $\approx$1 : 1 Gr/EC powder (Fig. S1, ESI†) in a solvent mixture of 90 : 10 ethanol/ethyl lactate, yielding a final ink composition containing a mass fraction of 2.86% Gr/EC solids (Fig. S2, ESI†). The viscosity of the ink was found to be 7.0 $\times$ 10^3 Pa s at a shear rate of 1000 s^{-1} (Fig. S3, ESI†), which makes this graphene ink formulation compatible with blade-coating and spin-coating. Following ink formulation, large-area Gr/EC films were blade-coated on SiO_2/Si substrates and polyimide substrates for Hall and microwave cavity measurements, respectively, followed by thermal curing at 300 °C for 30 min to decompose the EC binder into conducting films.

The Raman spectrum (Fig. 1a) of the resulting graphene films after thermal annealing exhibits a prominent G band at $\approx$1580 cm^{-1}, which is assigned to sp^2-rich carbon networks, weak D and D′ bands at $\approx$1346 cm^{-1} and $\approx$1620 cm^{-1}, respectively, due to defects in the EC carbonaceous residue, and a 2D band at $\approx$2700 cm^{-1} that corresponds to the overtone of the D band in graphitic materials.[29] The low D/G ratio of 0.37 indicates that the EC carbonaceous residue has a relatively low defect density and thus possesses a high degree of sp^2-carbon.[30] The graphene flakes in the thin film also adopt a nearly planar morphology that are parallel to the substrate, yielding dense, percolating graphene networks (Fig. S4, ESI†). Cross-sectional scanning electron microscopy (SEM) imaging shows a laminar structure of the graphene film (Fig. 1b). Evidence of the amorphous EC carbonaceous residue bridging the planar flakes is depicted in a higher magnification SEM image (Fig. S5, ESI†). Furthermore, C1s X-ray photoelectron spectroscopy (XPS) (Fig. S6, ESI†) provides additional characterization of the EC carbonaceous residues. In particular, following pyrolysis of the EC polymer, the sp^2-carbon XPS peak intensity increases significantly while the C–O component is drastically reduced, indicating that the EC residues are primarily composed of sp^2-carbon bonds.[31] These observations suggest that the EC carbonaceous residues interact with graphene flakes *via* π–π stacking, which is expected to promote efficient charge transport as will be verified below.

DC electrical conductivity

Hall voltage (V_{xy}) and magnetoresistance (R_{xx}) were measured for $\approx$500 nm thick graphene films on SiO_2/Si substrates at a

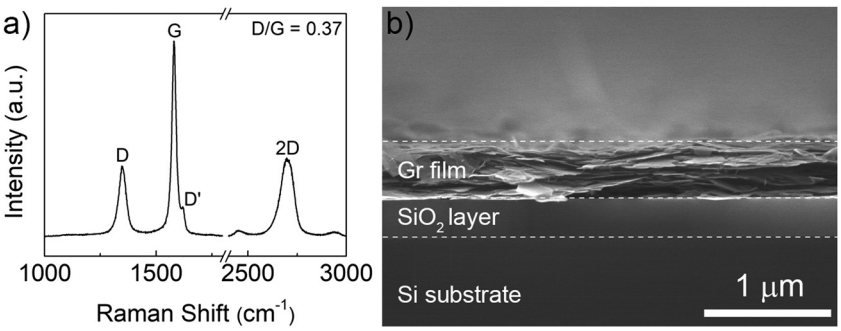

Fig. 1 (a) Raman spectrum of the graphene film after EC decomposition. (b) Cross-sectional SEM image of the graphene film deposited on a 300 nm SiO_2/Si substrate after EC decomposition.

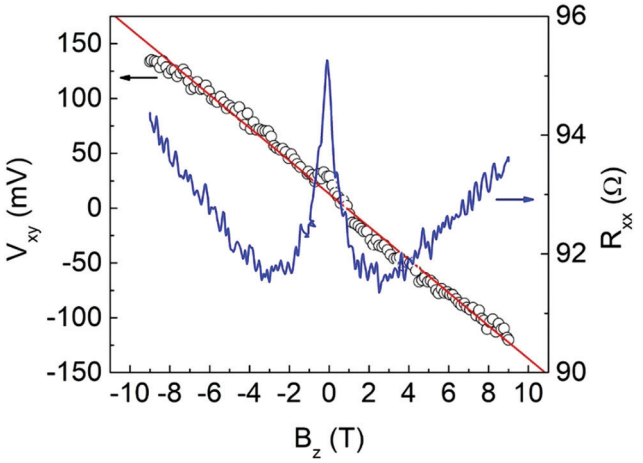

Fig. 2 Hall voltage (V_{xy}, open circles) as a function of magnetic field (B_z) at I_x of 1.0 μA and temperature of 5 K. The straight line represents a linear fit through the data points. The negative slope indicates that the majority charge carriers are holes. A characteristic peak in the plot of R_{xx} *versus* B_z is consistent with 2D charge transport, as discussed later.

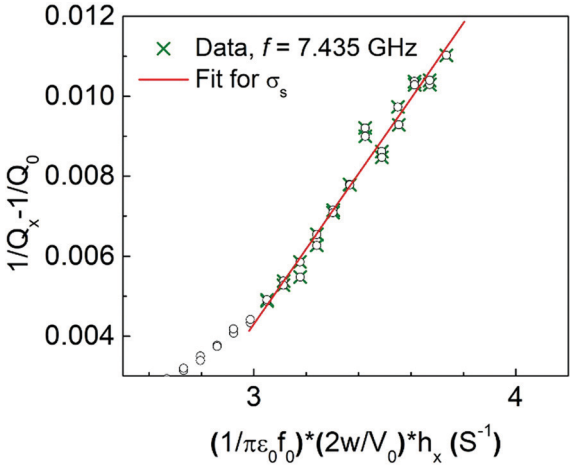

Fig. 3 Plot of cavity perturbation data ($1/Q_x - 1/Q_0$) as a function of the normalized specimen area ($w \times h_x$) for graphene inks at the resonant frequency of 7.435 GHz. Q_0 is the quality factor of the empty cavity, and Q_s is the quality factor of the cavity loaded with the specimen.[33] Symbols represent experimental data, and the solid line represents a linear fit to the cavity perturbation equation through the data points. In the presented notation, the microwave surface conductivity is obtained directly from the slope of the linear portion of the cavity perturbation plot, σ_s = (9.3 × 10^{-3} ± 3 × 10^{-4}) S.

temperature of 5 K (Fig. 2), resulting in the slope $d(V_{xy}/B_z)$ = −0.0152 V/T, R_{xx} (at 0 T) = 95.5 Ω, and I_x = 1.0 × 10^{-6} A. From these measurements, the mobility (μ) and density of charge carriers (n_p) are calculated to be $\mu = d(V_{xy}/B_z) \times 1/(I_x R_{xx})$ = (160 ± 8) $cm^2 V^{-1} s^{-1}$ (eqn (S4), ESI†) and $n_p = d(V_{xy}/B_z)(I_x/q)$ = (4 × 10^{14} ± 2 × 10^{13}) cm^{-2} (eqn (S5), ESI†), respectively. The negative slope of $d(V_{xy}/B_z)$ implies that the majority charge carriers are holes. The magnetoresistance peak in the R_{xx} plot of Fig. 2 indicates mixed metallic-semiconducting charge transport that can be attributed to charge carriers weakly localized by destructive quantum interference.[32] Similar localization occurs in large-area pristine graphene sheets. We note, however, that in the case of epitaxial monolayer graphene, the longitudinal resistance (R_{xx}) vanishes and the transverse resistance (R_{xy}) becomes quantized at high magnetic flux densities.[33] On the other hand, in the present case, the drop in R_{xx} observed in Fig. 2 when the magnetic flux changes from 0 T to ± 2 T appears to be much smaller, only about 4%, without evidence of quantized charge transport.

AC microwave conductivity

In addition to DC conductivity, AC conductivity was measured for ≈4 μm thick graphene films on polyimide substrates at a microwave frequency of 7.435 GHz using a non-contact microwave cavity method.[33] The measured AC microwave sheet conductance, σ_s = 9.26 × 10^{-3} S, is obtained directly from the slope of the linear portion of the plot shown in Fig. 3. When considering the ≈ 8-fold difference in thickness between the graphene films on SiO_2/Si *versus* polyimide, the measured AC microwave sheet conductance value is comparable to that obtained from the DC Hall measurement, where $1/R_{xx}$ is 1.25 × 10^{-3} S at 295 K. The observed frequency dispersion in conductivity can be attributed to the presence of traps and graphene flake edges, which causes localization of charge carriers due to dipolar-dielectric polarization.[34]

Temperature-dependent charge transport

Fig. S7 (ESI†) shows the DC longitudinal resistance measured in the temperature range from 1.5 K to 295 K. The resistance decreases continually with increasing temperature, indicating thermally activated charge transport and thus semiconducting character of the percolating graphene network. However, in contrast to the highly non-linear temperature behavior of conventional semiconductors, the decrease of R_{xx} with temperature above 50 K is essentially linear. The coefficient of thermal resistance (α) referenced to resistance R_0 = 78.9 Ω at 273 K (0 °C) is about −8.3 × 10^{-4}, which is comparable to carbon microstructural interfaces having both metallic and semiconducting properties.[35] We rule out the possibility of Mott variable range hopping (VRH) transport in favor of thermally activated charge transport since the activation energy does not show the expected temperature dependence for VRH (Fig. S8, ESI†).[36]

To further analyze the temperature dependence, the relative conductivity ($\sigma_r = 1/(R_{xx}/R_0)$) as a function of reciprocal temperature ($1/T$) is plotted in Fig. 4. The plot of $\ln(\sigma_r)$ as a function of $1/T$ (Fig. 4a) can be divided into three distinguishable temperature regions, where each region is fit to an Arrhenius model, $\sigma_r = \sigma_0 \exp(-E_g/2kT)$, with a different value of the activation energy (E_g) referenced to R_{xx} at 273 K. The three regions of transport are labelled with E_{g1}, E_{g2}, and E_{g3}.

In region 1, from 295 K to 50 K, the percolating graphene films show semiconducting character, with the electronic structure corresponding to a two-band model. The charge transport energy gap E_{g1} is ≈ 4.2 × 10^{-3} eV is comparable to few-layer graphene.[37] In this case, the mobility is likely to be affected by lattice scattering $\mu \propto T^{-3/2}$.[38] In region 2, which corresponds to

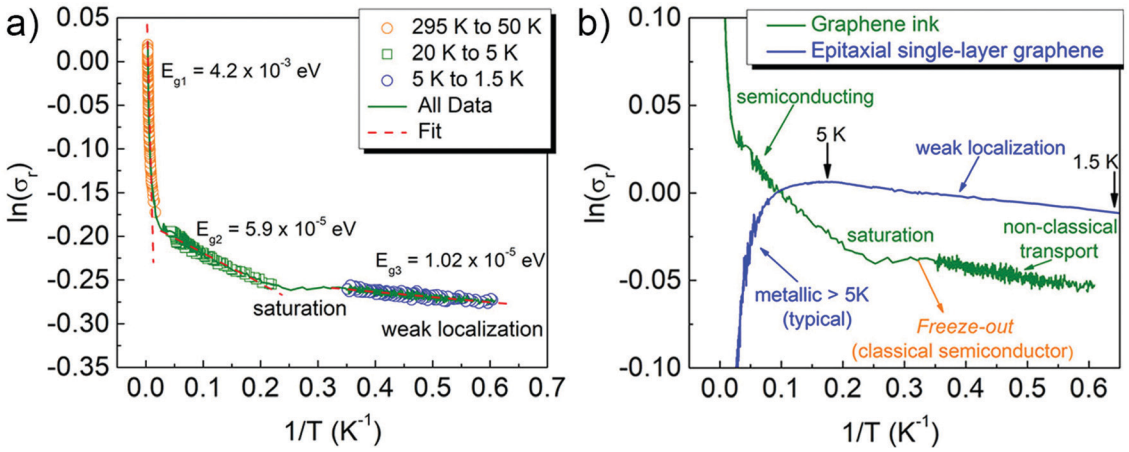

Fig. 4 (a) Logarithm of relative conductivity ($\sigma_r = 1/(R_{xx}/R_0)$) *versus* reciprocal temperature ($1/T$) referenced to R_{xx} at 273 K. (b) Comparison of the temperature-dependent conductivity of the percolating network generated from cellulose-stabilized graphene inks (green line) with that of epitaxial graphene with a carrier density of $\approx 2 \times 10^{11}$ cm^{-2} (blue line) referenced for clarity to R_{xx} at 10 K.

the temperature range from 20 K to 5 K, E_{g2} decreases by two orders of magnitude to $\approx 5.9 \times 10^{-5}$ eV, as the transport approaches the saturation region (Fig. 4a). The approximate temperature dependence of mobility due to lattice scattering in metallic conductors is $T^{-3/2}$. The impurity scattering in semiconductors results in the opposite effect, $\mu \propto T^{3/2}$. Therefore, in the case of mixed metallic-semiconducting transport, the temperature dependence of conductivity depends primarily on the charge carrier concentration. In other words, assuming a temperature-independent mobility μ,[39] σ_r is proportional to the density of charge carriers, n_p, and, therefore, this variable determines the temperature dependence of σ_r. In the saturation region below 5 K, the $\ln(\sigma_r)$ *versus* $1/T$ characteristic is relatively flat.

Considering the conductivity temperature dependence of a conventional semiconductor, n_p should depopulate and neutralize the dopants as the temperature decreases below the saturation range (below 5 K), resulting in a freeze-out region. In this case, σ_r should decrease rapidly towards an insulating state, as is illustrated in Fig. 4b. However, the experimental results shown in Fig. 4b suggest a considerable contribution to σ_r from 2D metallic charge carriers that remain mobile even at the lowest temperatures in a manner similar to single-layer graphene. This non-classical charge transport shows a remnant thermal activation with a small E_{g3} of $\approx 10^{-5}$ eV, comparable to that of epitaxial graphene (as shown in the blue plot in Fig. 4b),[33] which can be attributed to weak localization (WL).[28]

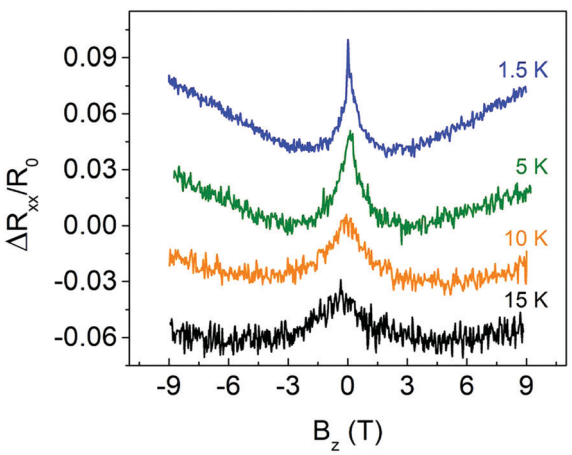

Fig. 5 Magnetoresistance of the percolating network generated from cellulose-stabilized graphene inks at the following temperatures: 1.5 K, 5 K, 10 K, and 15 K.

Magnetoresistance characterization

Fig. 5 shows the relative magnitude of magnetoresistance of the percolating graphene network ($(R_{xx} - R_0)/R_0$, where R_0 is the minimum value of R_{xx}) as a function of B_z at different cryogenic temperatures. A magnetoresistance peak at B_z near zero is consistent with the WL effect, indicating a certain degree of quantum coherence where the metallic carriers remain in phase over several mean free paths.[28] With increasing temperature, the WL peak decreases and becomes wider. These observations suggest that the phase coherence length decreases with temperature, that is, with increasing number of thermally activated holes, n_p (see the non-classical transport range in Fig. 4). At temperatures below 10 K, R_{xx} approaches a minimum value at about 1.2 T and −1.2 T, and then it increases again with increasing B_z. This magnetic field dependence is a signature of a weak anti-localization (WAL) effect arising from iso-spin in monolayer graphene.[40,41] Evidently, both types of carriers (electron and holes) having equal mobility exist at this condition. Consequently, at finite magnetic field, the net drift velocity orthogonal to the applied I_x causes this weak anti-localization effect to appear.[42]

Conclusions

In summary, we have systematically characterized the charge transport mechanisms in percolating networks generated from cellulose-stabilized graphene inks. These graphene films show high mobility, low energy gap, and weak localization behavior akin to monolayer graphene at cryogenic temperatures.

From DC charge transport measurements, a hole mobility of $\approx$160 cm^2 V^{-1} s^{-1} is extracted, which is exceptionally high compared to other solution-processed graphene films, thus highlighting the importance of the sp^2-rich amorphous carbon residue from the cellulosic polymer in facilitating charge transport between graphene flakes. Furthermore, non-contact microwave cavity measurements confirm that the sheet conductance of these percolating graphene networks remains high up to GHz frequencies, which suggests the utility of these graphene films for microwave frequency applications. In the ultralow temperature limit, these graphene films also show temperature-dependent conductivity that is comparable to epitaxial graphene monolayers, which further corroborates the exceptional charge transport characteristics of percolating networks generated from cellulose-stabilized graphene inks. Overall, this work suggests that printed films based on cellulose-stabilized graphene inks are suitable for a diverse range of high-performance electronic applications.

Conflicts of interest

The authors declare no conflict of interest.

Acknowledgements

This work was primarily supported by the U.S. Department of Commerce, National Institute of Standards and Technology (Award 70NANB19H005) as part of the Center for Hierarchical Materials Design (CHiMaD). Graphene powder production was supported by the National Science Foundation Scalable Nanomanufacturing Program (NSF CMMI-1727846). SEM and XPS characterization were performed in the Northwestern University Atomic and Nanoscale Characterization Experimental Center (NUANCE) facility, which is supported by the National Science Foundation (NSF) Soft and Hybrid Nanotechnology Experimental (SHyNE) Resource (NSF ECCS-1542205), the Materials Research Science and Engineering Center (MRSEC) (NSF DMR-1720139), the State of Illinois, and Northwestern University. Rheometry and thermogravimetric analysis were performed in the Materials Characterization and Imaging (MatCI) Facility, which receives support from the NSF MRSEC Program (NSF DMR-1720139). Electrical characterization was performed at the National Institute of Standards and Technology, Material Measurement and Physical Measurement Laboratories.

Notes and references

1 A. K. Geim and K. S. Novoselov, *Nat. Mater.*, 2007, **6**, 183–191.
2 S. V. Morozov, K. S. Novoselov, M. I. Katsnelson, F. Schedin, L. A. Ponomarenko, D. Jiang and A. K. Geim, *Phys. Rev. Lett.*, 2006, **97**, 016801.
3 K. S. Novoselov, V. I. Fal'ko, L. Colombo, P. R. Gellert, M. G. Schwab and K. Kim, *Nature*, 2012, **490**, 192–200.
4 D. Jariwala, V. K. Sangwan, L. J. Lauhon, T. J. Marks and M. C. Hersam, *Chem. Soc. Rev.*, 2013, **42**, 2824–2860.
5 J. Kang, V. K. Sangwan, J. D. Wood and M. C. Hersam, *Acc. Chem. Res.*, 2017, **50**, 943–951.
6 X. D. Duan, C. Wang, A. L. Pan, R. Q. Yu and X. F. Duan, *Chem. Soc. Rev.*, 2015, **44**, 8859–8876.
7 F. Bonaccorso, A. Lombardo, T. Hasan, Z. P. Sun, L. Colombo and A. C. Ferrari, *Mater. Today*, 2012, **15**, 564–589.
8 J. Zhu and M. C. Hersam, *Adv. Mater.*, 2017, **29**, 1603895.
9 V. Nicolosi, M. Chhowalla, M. G. Kanatzidis, M. S. Strano and J. N. Coleman, *Science*, 2013, **340**, 1226419.
10 G. Hu, J. Kang, L. W. T. Ng, X. Zhu, R. C. T. Howe, C. G. Jones, M. C. Hersam and T. Hasan, *Chem. Soc. Rev.*, 2018, **47**, 3265–3300.
11 J.-W. T. Seo, J. Zhu, V. K. Sangwan, E. B. Secor, S. G. Wallace and M. C. Hersam, *ACS Appl. Mater. Interfaces*, 2019, **11**, 5675–5681.
12 Y. Aleeva and B. Pignataro, *J. Mater. Chem. C*, 2014, **2**, 6436–6453.
13 E. B. Secor and M. C. Hersam, *J. Phys. Chem. Lett.*, 2015, **6**, 620–626.
14 E. B. Secor, S. Lim, H. Zhang, C. D. Frisbie, L. F. Francis and M. C. Hersam, *Adv. Mater.*, 2014, **26**, 4533–4538.
15 E. B. Secor, P. L. Prabhumirashi, K. Puntambekar, M. L. Geier and M. C. Hersam, *J. Phys. Chem. Lett.*, 2013, **4**, 1347–1351.
16 W. J. Hyun, E. B. Secor and M. C. Hersam, *MRS Bull.*, 2018, **43**, 730–733.
17 Y. T. Liang and M. C. Hersam, *J. Am. Chem. Soc.*, 2010, **132**, 17661–17663.
18 M. Lotya, Y. Hernandez, P. J. King, R. J. Smith, V. Nicolosi, L. S. Karlsson, F. M. Blighe, S. De, Z. Wang, I. T. McGovern, G. S. Duesberg and J. N. Coleman, *J. Am. Chem. Soc.*, 2009, **131**, 3611–3620.
19 T. Shen, J. J. Gu, M. Xu, Y. Q. Wu, M. L. Bolen, M. A. Capano, L. W. Engel and P. D. Ye, *Appl. Phys. Lett.*, 2009, **95**, 172105.
20 K. S. Novoselov, A. K. Geim, S. V. Morozov, D. Jiang, Y. Zhang, S. V. Dubonos, I. V. Grigorieva and A. A. Firsov, *Science*, 2004, **306**, 666–669.
21 A. Behnam, J. L. Johnson, Y. An, A. Biswas and A. Ural, *ACS Nano*, 2011, **5**, 1617–1622.
22 T. Juntunen, H. Jussila, M. Ruoho, S. H. Liu, G. H. Hu, T. Albrow-Owen, L. W. T. Ng, R. C. T. Howe, T. Hasan, Z. P. Sun and I. Tittonen, *Adv. Funct. Mater.*, 2018, **28**, 1800480.
23 G. Calabrese, L. Pimpolari, S. Conti, F. Mavier, S. Majee, R. Worsley, Z. H. Wang, F. Pieri, G. Basso, G. Pennelli, K. Parvez, D. Brooks, M. Macucci, G. Iannaccone, K. S. Novoselov, C. Casiraghi and G. Fiori, *Nanoscale*, 2020, **12**, 6708–6716.
24 A. F. Rigosi, C. I. Liu, B. Y. Wu, H. Y. Lee, M. Kruskopf, Y. F. Yang, H. M. Hill, J. N. Hu, E. G. Bittle, J. Obrzut, A. R. H. Walker, R. E. Elmquist and D. B. Newell, *Microelectron. Eng.*, 2018, **194**, 51–55.
25 A. F. Rigosi, N. R. Glavin, C. I. Liu, Y. F. Yang, J. Obrzut, H. M. Hill, J. N. Hu, H. Y. Lee, A. R. H. Walker, C. A. Richter, R. E. Elmquist and D. B. Newell, *Small*, 2017, **13**, 1700452.
26 U. Mogera, S. Walia, B. Bannur, M. Gedda and G. U. Kulkarni, *J. Phys. Chem. C*, 2017, **121**, 13938–13943.
27 N. García, P. Esquinazi, J. Barzola-Quiquia and S. Dusari, *New J. Phys.*, 2012, **14**, 053015.

28 S. V. Morozov, K. S. Novoselov, M. I. Katsnelson, F. Schedin, L. A. Ponomarenko, D. Jiang and A. K. Geim, *Phys. Rev. Lett.*, 2006, **97**, 016801.
29 M. A. Pimenta, G. Dresselhaus, M. S. Dresselhaus, L. G. Cançado, A. Jorio and R. Saito, *Phys. Chem. Chem. Phys.*, 2007, **9**, 1276–1290.
30 D. Song, E. B. Secor, Y. Wang, M. C. Hersam and C. D. Frisbie, *ACS Appl. Mater. Interfaces*, 2018, **10**, 22303–22310.
31 M. J. Obrzut and F. E. Karasz, *Macromolecules*, 1989, **22**, 458–464.
32 A. A. Lebedev, N. V. Agrinskaya, V. A. Berezovets, V. I. Kozub, S. P. Lebedev, A. A. Sitnikova and D. A. Kirilenko, *Mater. Sci. Forum*, 2013, **740-742**, 137–140.
33 J. Obrzut, C. Emiroglu, O. Kirillov, Y. F. Yang and R. E. Elmquist, *Measurement*, 2016, **87**, 146–151.
34 J. Obrzut and K. A. Page, *Phys. Rev. B: Condens. Matter Mater. Phys.*, 2009, **80**, 195211.
35 N. Garcia, P. Esquinazi, J. Barzola-Quiquia and S. Dusari, *New J. Phys.*, 2012, **14**, 053015.
36 N. F. Mott, *Metal-insulator transitions*, Taylor & Francis, London, New York, 2nd edn, 1990.
37 K. Nagashio, T. Nishimura, K. Kita and A. Toriumi, *Jpn. J. Appl. Phys.*, 2010, **49**, 051304.
38 S. O. Kasap, *Principles of electronic materials and devices*, McGraw-Hill, Boston, 3rd edn, 2006.
39 J.-H. Chen, C. Jang, S. Xiao, M. Ishigami and M. S. Fuhrer, *Nat. Nanotechnol.*, 2008, **3**, 206–209.
40 X. S. Wu, X. B. Li, Z. M. Song, C. Berger and W. A. de Heer, *Phys. Rev. Lett.*, 2007, **98**, 136801.
41 Y. F. Chen, M. H. Bae, C. Chialvo, T. Dirks, A. Bezryadin and N. Mason, *Phys. B*, 2011, **406**, 785–788.
42 E. H. Hwang, S. Adam and S. D. Sarma, *Phys. Rev. Lett.*, 2007, **98**, 186806.